Sandia National Laboratories

Operated for the U.S. Department of Energy's
National Nuclear Security Administration

by **Sandia Corporation**

Albuquerque, New Mexico 87185

date: January 10, 2014

to: Leanna Minier, Org. 2554

from: Marvin E. Larsen, John Tencer, and Roy E. Hogan, Org. 1514

subject: Summary of MgO Bag and Room Model Team

Executive Summary

The salt truck fire of February 5th introduced heating to the mine air and resulted in reduction of the total airflow through the mine during the process of personnel evacuation. Both of these effects have the potential to slightly diminish cooling to the waste array. The temperature increase in Panel 7 Room 7 (P7R7) air temperature during the fire was estimated to be less than 5°C. Drum 68660 is inside the waste array and its interior would not be expected to respond to the small and temporary temperature increase of air at the waste array boundary. The convective coupling at the edge of the waste array is associated with very small heat flux so that the edge of the waste array would remain very near the temperature of the passing air even as the convection coefficient was diminished by reduced flow velocity. The magnitude of the P7R7 air temperature increase and the increase in temperature at the edge of the waste array associated with diminished flow could be small contributing factors to the incubation of an escalating reaction. However, these temperature increases are small compared to the temperature variations expected in the normal handling of the waste drums in the course of their prior storage, shipping, and handling to emplace at WIPP. Consequently, it is judged that these factors were not causal.

Given the energetic output predicted by the thermochemical runaway calculation for Drum 68660, the CFD calculation demonstrated that it is plausible that the barrel's hot effluent in the cross-flow could reach much of the area known to be damaged. Other mechanisms such as combustion in the room, flame propagation, burning drips of melted polymer and hot solid ejected material from the drum may also have contributed to the spreading of thermal damage. Unknown flow characteristics, dependent upon geometry details that are altered in the aftermath, and unknown distribution of combustible and low-melting point materials prior to the damaging event preclude the possibility of developing a precise description of thermal damage event.

Transient thermal analyses demonstrated that drum-to-drum propagation would require extremely energetic donor drums to significantly heat neighbor drums. Further, the thermochemical analyses demonstrating a plausible thermal runaway condition require isolation of the exothermic reaction within a region of low thermal diffusivity. Consequently, it is believed that the thermal stimulus leading to the pressurizing and failure of Drum 68660 was internal. The expulsion of energy from Drum 68660 most likely initiated the observed damage to the surrounding area and not vice versa.

Introduction

On February 5, 2014, at approximately 10:48 AM, there was an underground fire in a salt hauler vehicle at the Department of Energy (DOE) Waste Isolation Pilot Plant (WIPP) near Carlsbad, New Mexico. An accident investigation board was appointed to investigate the accident. That investigation lasted from February 10, 2014 through March 8, 2014 and the findings are summarized in the resulting report[1]. Nine days after the truck fire event a radiological release occurred at the WIPP site on February 14, 2014. Because of the close proximity of the two events, a causal relationship was posited.

The truck fire occurred in the E-0 drift at the intersection with the drift and N-300. The fire was limited to the forward half of the vehicle and consumed two tires and most of the available combustible liquids as shown in Figure 1.

Figure 1: Salt hauling truck after the fire

The occurrence of the February 14, 2014 radiation release in Panel 7 Room 7 (P7R7), less than 10 days after the February 5 salt haul truck fire, raises suspicion that the two events may be related. Figure 2 shows a perspective view of the mine system indicating the location of the truck fire, the location at which the radiological release was first detected, and P7R7.

There are a number of ways that these two events could be related to each other, including heat and/or combustion products from the fire being transported into P7R7. Additionally, the flow of air through P7R7 was reduced for a period after the truck fire which potentially could have reduced the cooling of the waste array, leading to overheating of particular drums. Analyses for each of these potential scenarios follow.

---

[1] U.S. Department of Energy Office of Environmental Management Accident Investigation Report, *Underground Salt haul Truck Fire at the Waste Isolation Pilot Plant February 5, 2014*, March 2014.

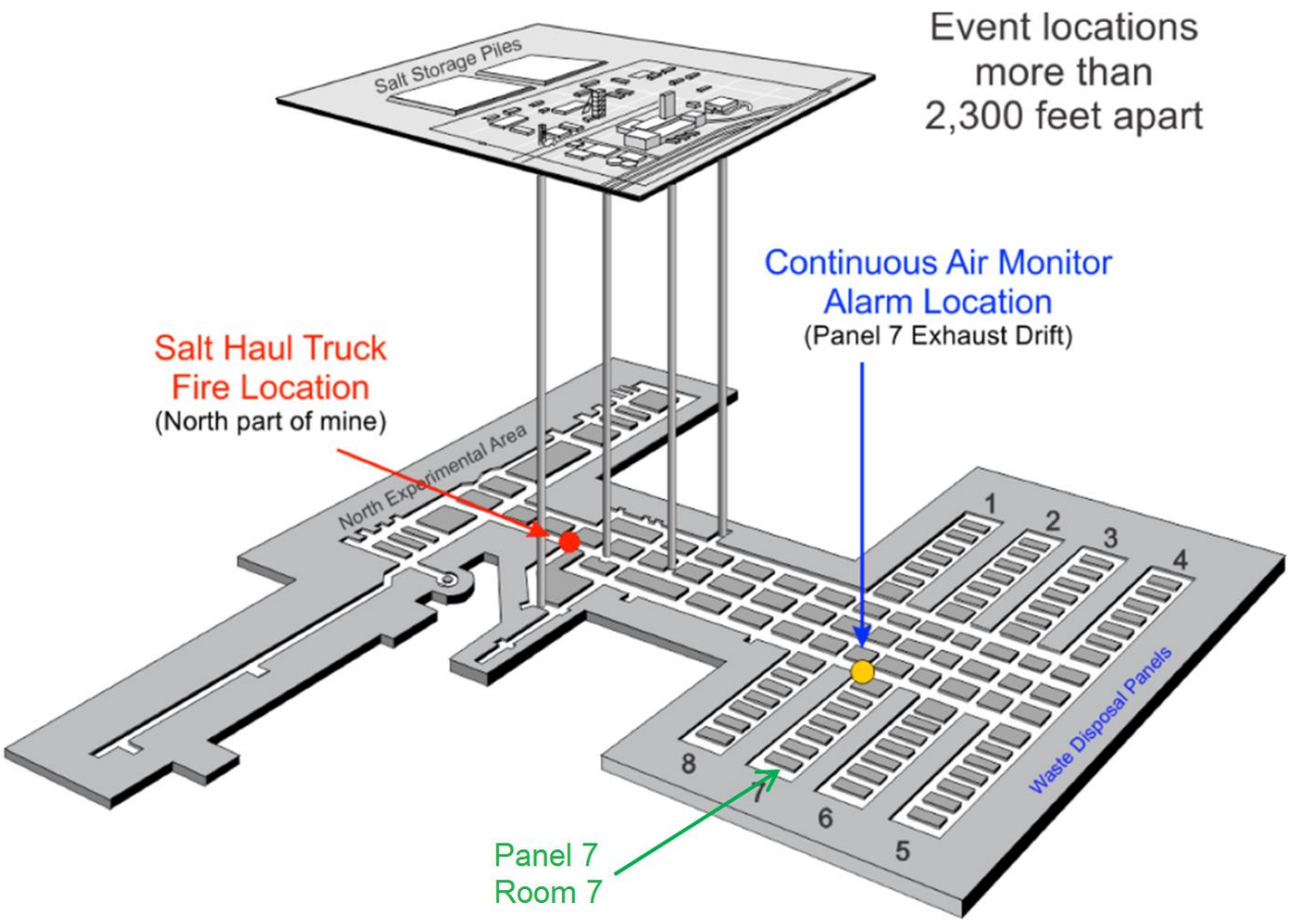

Figure 2: Fire and radiological event locations

Specific Questions to be Addressed

This memo documents analyses by the MgO bag sub team of the TAT assessing the plausibility of a number of different scenarios in which the MgO bags may have participated in or contributed to the radiological release event in P7R7 at WIPP. In addition to addressing the bag damage, several other questions were analyzed by this team. The sections are written with the intent of this material contributing to a larger, more comprehensive TAT report. Consequently, the following sections in this memo are nearly "stand-alone" summaries of analyses addressing specific questions.

The specific questions that are investigated here are:

- Could the February 5 fire involving the Salt Haul Truck (SHT) have any significant influence on Panel 7 Room 7 resulting radiation release? Three possible mechanisms were considered:
  - Thermal: Did heating from the fire significantly heat the waste array?
  - MgO Reactions: Could CO_2 or H_2O from fire combustion products stimulate an exothermic reaction in the MgO on the waste array?
  - Did reduced flow through the waste array result in significant heating?
- Could the release from drum 68660 alone have caused the damage observed to the MgO sacks and the slip sheets?
- Can we estimate the time duration of the release event based on measured radiological data?

The following sections summarize analyses conducted by the MgO team to address the questions above, as well as several other related questions of interest. To address the questions above, simplifying assumptions had to be employed because there is significant uncertainty in the actual conditions within the room and waste pack, i.e. mass flows, waste-pack geometry, temperatures, etc. In many cases, the computed results from a numerical model will depend strongly on the boundary conditions. It is necessary to have well-known properties and boundary conditions to have high confidence in the computed results. One way of handling the large uncertainty in the specific problem is to rely on simplified or bounding analyses. Using bounding analyses, it may be feasible to develop some insight into the system response that could be used to demonstrate or eliminate the plausibility of specific physical mechanisms. Our approach for addressing the large uncertainty was to focus on assessing the plausibility of specific physical mechanisms, rather than attempting to compute an "exact" response. The level of detail in the analyses employed was limited by the tight time schedule for completing the project, which initially was expected to have been completed in October, 2014.

Influence of the February 5 Salt Haul Truck Fire

This analysis demonstrates that the truck fire could not have resulted in significant heating of P7R7. Reports[2] of undamaged materials with low melting points both in the waste array and nearer the truck location indicated that very high temperatures (>~130°C) had not occurred anywhere near P7R7. Available data to support the analysis includes temperatures and air flow rates recorded by the mine's Central Monitoring System (CMS).

Smoke was seen issuing from the salt handling shaft (SHS) confirming that there was outflow from that shaft after the fire. It is evident from recorded temperatures that the SHS was acting as an air supply prior to the fire. The analysis finds air mass flows for the air intake shaft (AIS) and SHS that balance friction losses with buoyancy differences associated with temperature differences in the two shafts while requiring the exit air temperature of the SHS to match the measurement. The recorded temperature of air leaving through the SHS was only around 30°F higher than the ambient air at the time of the fire. The analysis demonstrates that 62°C is a conservatively high estimate of the air temperature at the base of the SHS. Given this upper bound on air temperature at the base of the SHS, further conservative assumptions are made regarding energy loss from air in transit to P7R7 and it is shown that the temporary increase in air temperature arriving at the waste array was less than 5°C.

The ambient air temperature for early February used in the analysis was taken from historical data for the city of Carlsbad. The temperature recorded for air entering the SHS by the CMS was a few degrees colder than the historical data immediately prior to the fire. The effect of adjusting the ambient temperature prior to the fire downward (to agree with the CMS) would result in slightly higher estimates of the temperature at the base of the SHS and a negligible influence on the temperature estimated for P7R7.

Thermal Analysis of Fire Influence

Upcasting Through the Salt Handling Shaft During/After Fire

In normal operation the air inlet shaft (AIS) and salt handling shaft (SHS) are air supplies to the WIPP mine system. After the initiation of the fire of February 5 at WIPP the SHS reversed flow due to the

[2] Draft reports were shared by AIB analysts that included descriptions of materials proximal to but not melted by the fire. Analyses in this memo also utilize from AIB draft reports: pre-fire ventilation air flow rates of 142 kg/s, AIS and SHS shaft diameters of 6.25 and 3.05 m respectively, and 5 and 10 MW fire thermal output estimates.

buoyancy of the heated air at the lower end of the shaft. Figure 3 below is visual evidence of the flow reversal.

Figure 3: Smoke exiting the salt shaft[3]

Figure 4 shows the recorded temperature near the top of the salt handling shaft from 10:00 a.m. on the morning of the 5th through the next day. The vertical red line corresponds to the time of the onset of the fire (10:48). Prior to the fire the SHS is acting as an inlet to the mine system and the indicated temperature is in reasonable agreement with Carlsbad temperatures shown in Figure 5. The CMS record indicates an upturn of the SHS exiting air temperature starting at 1102, just a few minutes after the ventilation mode was switched. In the hour following the fire onset, the temperature recorded near the SHS top increases approximately 20°F. This is evidently due to the flow reversal. The speed of the established, reversed flow was estimated to be about 9 m/s, for which the transit time for air entering the bottom shaft to arrive at the top would be approximately 72 s. Apparently the walls of the SHS, having been cold-soaked for days, cool the upcasting air but gradually the shaft wall warms up. After the first hour the temperature continues to rise about another 3°F over 12 hours. It appears that the fire is out in this interval but the flow is gradually warming as the walls of the shaft slowly warm due to mine-level warmer air passing. Just before midnight on the 5th the flow reverses again due to adjustments made to the ventilation system.

An analysis was conducted to estimate airflow in the SHS after the fire. Flow velocities are estimated that balance the effects of buoyancy and friction for the flow conditions that were seen following the fire. Specifically, during an interval after the fire, the air in the SHS is warmer than that in the AIS and there is a buoyantly driven flow out the SHS. The AIS supplies the SHS flow and the flow removed from the mine by the ventilation system. The buoyant force is balanced by friction losses in both shafts. Conservation of energy is considered for air flowing into the shafts and for geologic material constituting the shaft walls.

---

[3] U.S. Department of Energy Office of Environmental Management Accident Investigation Report, *Underground Salt haul Truck Fire at the Waste Isolation Pilot Plant February 5, 2014*, March 2014.

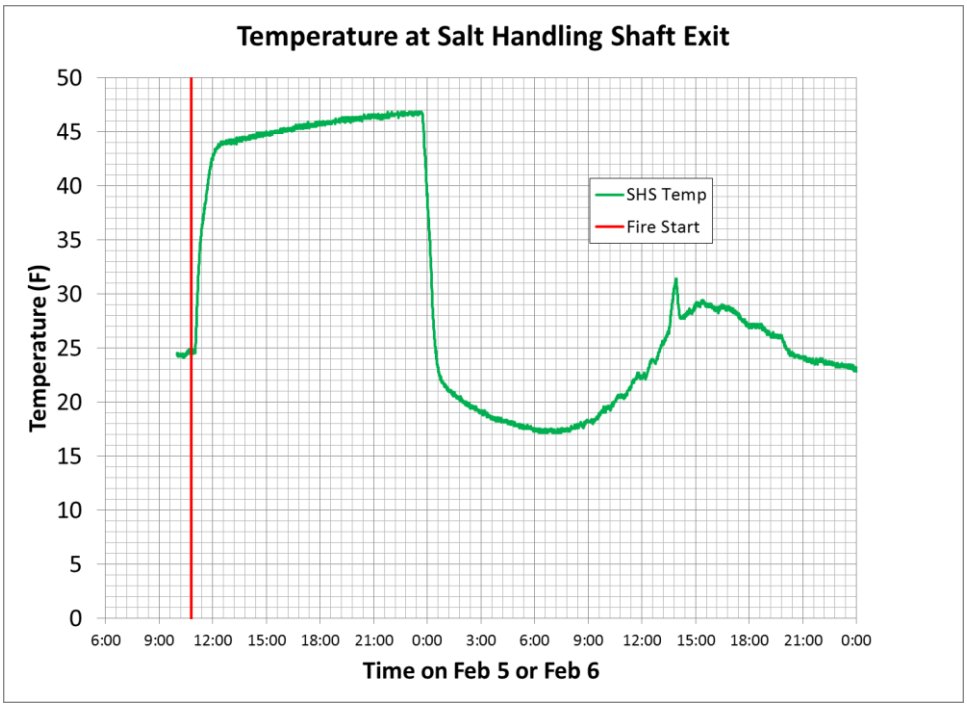

Figure 4: Temperature near the top of the salt handling shaft on February 5th and 6th

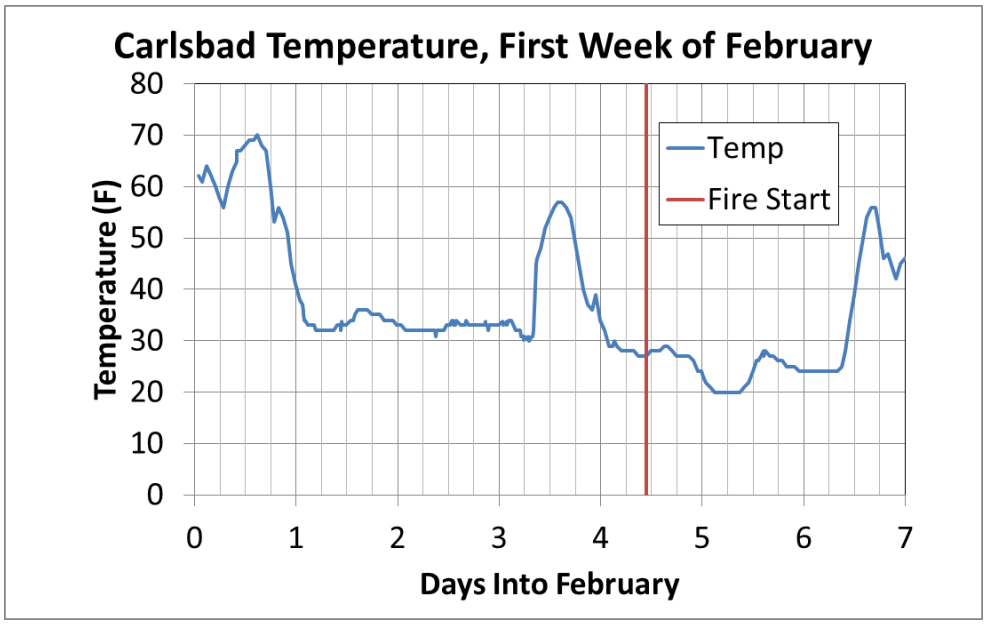

Figure 5: Carlsbad temperatures in early February[4]

4 http://www.wunderground.com/history/airport/KCNM/2014/2/5/DailyHistory.html?req_city=NA&req_state=NA&req_statename=NA This link provides hourly weather for February 5, 2014. The weather data was constructed by visiting each early day in February and electing the provision for comma-separated data export.

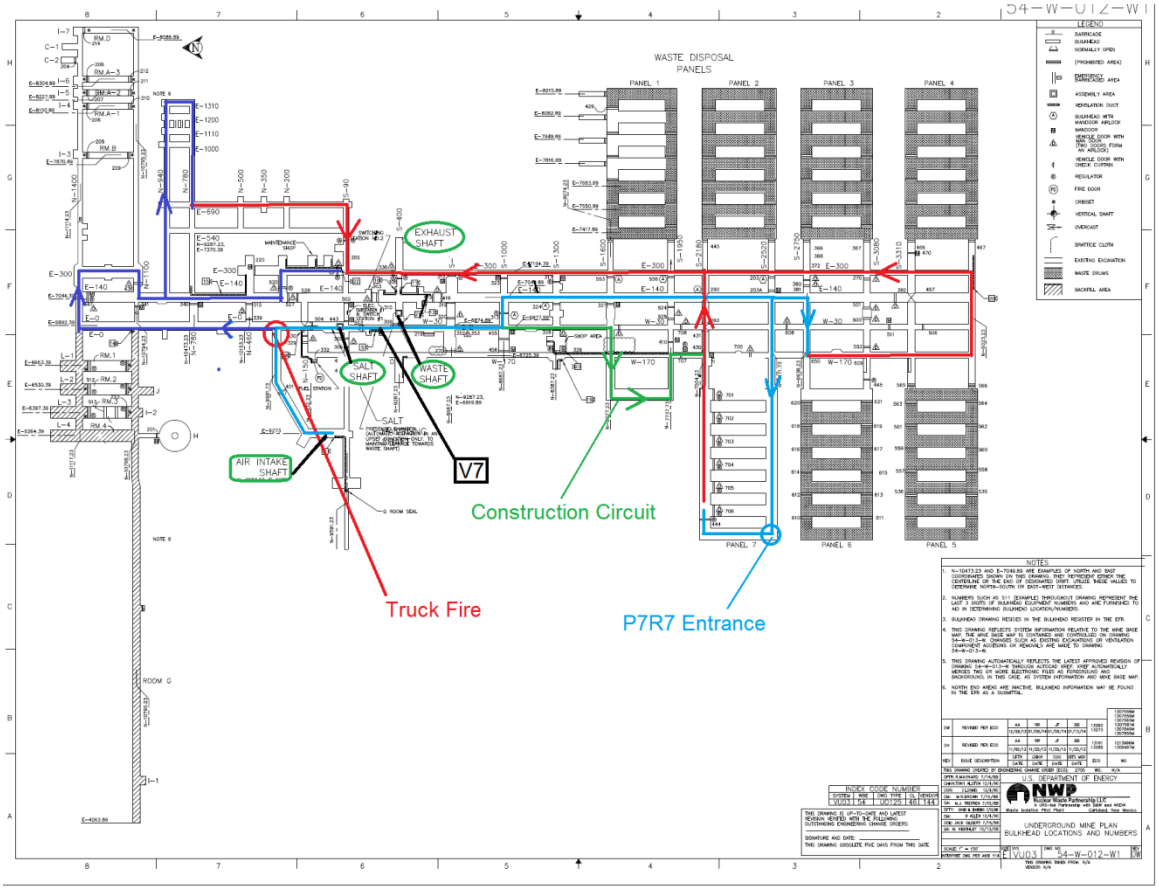

Figure 6: Plan view showing principal mine relationships of air inlet shaft, truck fire, and P7R7

Figure 6 shows principal flow circuits in the mine system. Approximately ten minutes after the fire started on the 5th of February the total flow through the mine system was reduced with the expectation of limiting the travel of smoke from the fire. The 142 kg/s pre-fire flow rate that will be used in the following analysis corresponds to the flow indicated by the CMS for V7 prior to the fire.

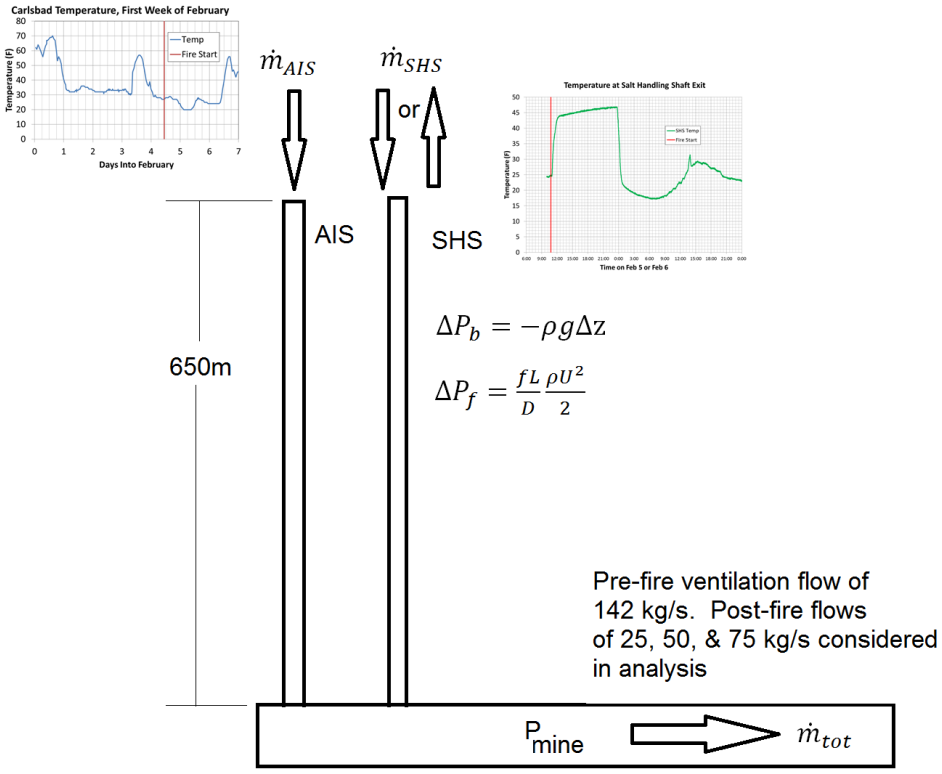

Figure 7: WIPP flow model schematic

Flow Analysis

Figure 7 shows a schematic rendering of the flow model. Some of the flow from the AIS went through the north circuit and energy deposited there could only help reduce heating in the direction towards Panel 7. However, for this analysis, the bulk of the flow heads south and the north circuit is flow is neglected. The pressure change due to friction between two positions along an interval (Δz) of flow in a shaft is estimated as:

$$\Delta P_f = \frac{f\Delta z}{D}\frac{\rho U^2}{2} \quad (1)$$

The friction factor, f, was evaluated such that it satisfy the Colebrook formula. Properties of dry air were used for the analyses. Temperature dependent viscosity and thermal conductivity were included. The pressure change due to buoyancy force is:

$$\Delta P_b = -\rho g \Delta z \quad (2)$$

The AIS and SHS shafts were discretized into 40 vertical intervals and Eqs. 1 and 2 were applied to successive intervals in the direction of flow. At each segment the local density for air was calculated using the inlet temperature and pressure of the air. Heat exchange was considered between the flowing air and the bounding wall such that:

$$T_2 = T_W + (T_1 - T_w) \times \exp(-\frac{h\pi D\Delta z}{\dot{m}C_p}) \quad (3)$$

where T_W is the average of the wall temperature at the segment entrance and exit; T_1 and T_2 are the entrance and exit air temperatures; and $\dot{m}$ is the mass flow rate. h is the convection coefficient and D the diameter. Equation (3) is applied to one axial segment at a time (~16 m length) so the associated constant wall temperature of the model is reasonable. The total heat transfer between the air and the wall for the interval is then:

$$Q = \dot{m}C_p(T_2 - T_1) \quad (4)$$

Q was then applied as a uniform boundary flux for a simple finite difference model of transient radial conduction into or out of the geologic media forming the shaft wall. An annulus of material 1-m thick was considered which was divided into 40 radial segments[5]. Axial conduction was not considered and at the outside radius of the conduction system the boundary was considered adiabatic. Temperatures were associated with the 41 faces bounding the 40 radial layers for the midpoints of each of the 40 axial intervals. Consequently, each of the AIS and SHS had 1640 associated transient temperatures. Simple conduction with constant thermal conductivity was used to derive thermal resistance between successive layers. Any excess conduction in a layer (more energy in from the neighbor than out to the next neighbor) is available for increasing the local temperature. The resulting 3280 first-order differential equations were integrated through time using the Runge-Kutta method[6]. **Error! Reference source not found.** shows a schematic representation of the transient radial conduction system that applies for each axial segment of the model.

[5] A transient analytical solution for a semi-infinite material suddenly subjected to a convective heating boundary was examined to determine small response at about 1-m depth for 12 hours of heating. The choice is somewhat arbitrary but this thickness is sufficient to provide a boundary region in which the outer part only exhibits a small response relative to the surface temperature variations associated with the diurnal variation of the local weather.

[6] Felberg, E. NASA TR R-315 (1969).

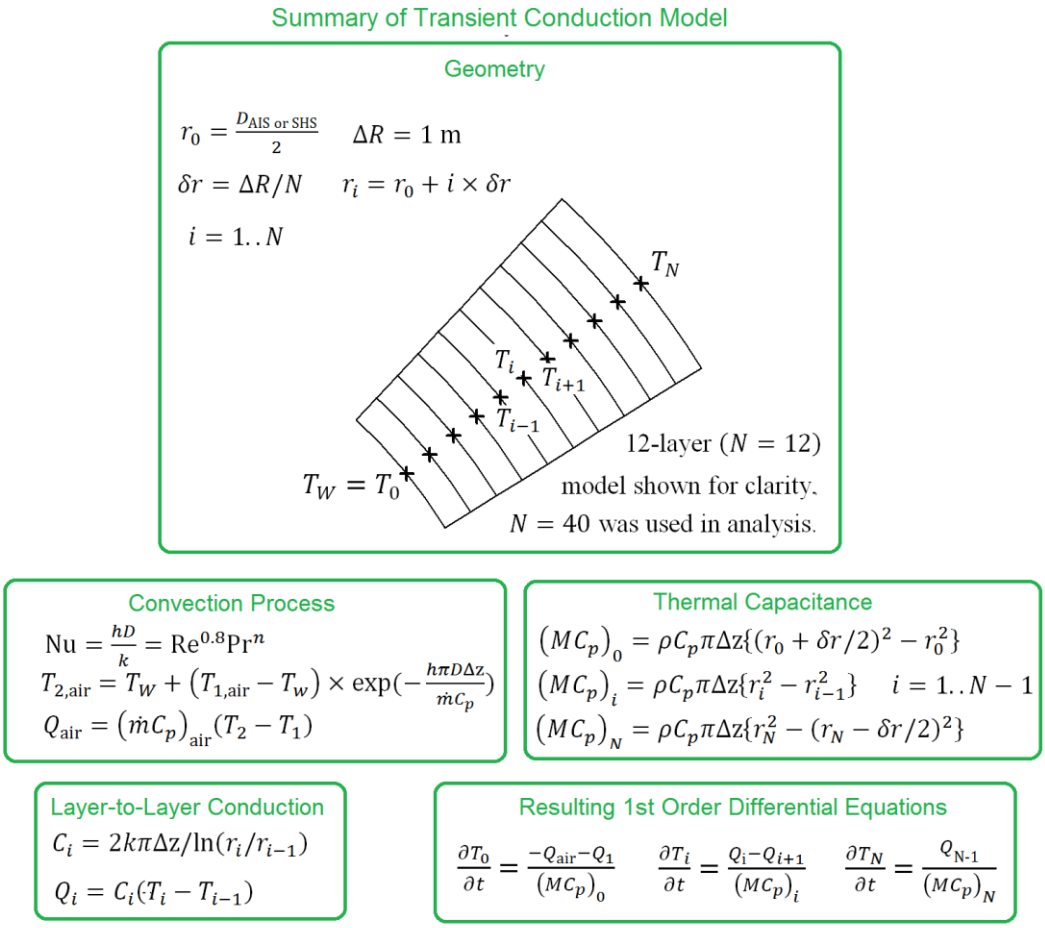

Figure 8: Geometry of an axial segment in transient conduction model.

The strata traversed by the shafts undoubtedly exhibit appreciable variation in thermal properties. Thermal properties of the lithosphere were taken as constant for convenience and representative of the earth in general. The analysis could possibly be improved by using depth-appropriate property adjustments along the shafts. The constant values of $k = 3\text{W}\cdot\text{m}^{-1}\cdot\text{K}^{-1}$, $\rho = 2800$ kg·m^{-3}, and $C_p = 1000$ J·kg^{-1}·K^{-1} were used for the properties of the earth forming the shafts. Nonetheless, the character of the system of ventilated shafts through geologic media is represented in the model and more precise specification of shaft wall properties would not be expected to significantly change the results.

A uniform initial temperature was assigned (275K, ~2°C) to the conduction system and the integration was started at 12:00 a.m. on February 1 so that the first 4 and half days up to the fire onset were to establish an initialized condition for the material in the conduction system. The entrance air temperature for both shafts prior to the fire was that in Figure 5.

The convective coefficient between the air and the shaft wall, h, was estimated using the Dittus-Boelter Equation:

$$\text{Nu} = \frac{hD}{k} = \text{Re}^{0.8}\text{Pr}^n \qquad (5)$$

where the exponent on the Prandtl number is 0.3 when the air is cooled by the wall and 0.4 when it is heated.

Prior to the fire, both shafts are inlets and the sum of their flows equals the ventilation system flow[7] which was taken to be constant at 142 kg/s. For either shaft the analysis steps from the surface to the mine successively applying all of Eqs. 1-5 to march down the shaft. For these conditions the magnitude of the sum of the ΔP_f from Eq. 1 is very much less that of ΔP_b. Consequently, it was problematic to find a division of the mass flow that resulted in a matching pressure at the bottom ends of the shafts. The actual initial conditions for the rock were not known and the shafts having two different diameters result in different heating rates. Because the ΔP_f contribution to the pressure change going down the shaft was small, the equilibrium condition was fickle with regard to the unknown temperature distribution. So, rather than requiring precise agreement in pressure at the bottom of the two shafts, the flow was divided so that the total friction pressure drop was the same in both shafts assuming the same friction factor. That is:

$$\left(\frac{fL}{D}\frac{\rho U^2}{2}\right)_{SHS} = \left(\frac{fL}{D}\frac{\rho U^2}{2}\right)_{AIS} \tag{6}$$

Requiring the pressure to be the same on both ends of both shafts and their friction losses to be the same likewise requires that the integrated effect of buoyancy be the same for the two shafts (neglecting the small difference associated with exit losses of two different velocities). This result depends on the shaft diameters and results in the constant division of flow:

$$\dot{m}_{AIS} = \frac{\dot{m}_{tot} A_{AIS}}{\left\{\sqrt{\frac{D_{SHS}}{D_{AIS}}} A_{SHS} + A_{AIS}\right\}} \tag{7}$$

and

$$\dot{m}_{SHS} = \dot{m}_{vent} - \dot{m}_{AIS} \tag{8}$$

The condition of Eq. (7) was used to divide the flow until the time of the fire. For the diameters of 6.25 and 3.05 m, used to characterize the AIS and SHS, approximately 85% of the pre-fire total mass flow was through the AIS. After the fire, ($\dot{m}_{AIS}$) must supply both the ventilation flow ($\dot{m}_{Vent}$) and the flow that goes up the salt handling shaft ($\dot{m}_{SHS}$). Specification of flow past the SHS is poorly understood, so in the post-fire analysis $\dot{m}_{Vent}$ is treated as a parameter. Analyses are completed for 25, 50, and 75 kg/s flows.

The flow in the SHS and the temperature at its base are unknown. Newton's method was used to search on these two variables to find conditions that satisfy the requirements that the pressure at the mine level is the same for both shafts and the exiting air temperature for the SHS matches the record in Figure 4. Solutions to the flow as formulated were not found until about 20 minutes after the 1048 report of the fire onset. (The solution conditions could not be met for the very lowest measured SHS outlet

[7] Several quantities used in the current analysis were taken from a preliminary analysis shared by AIB analysts. These include: the ventilation air flow rates of 142 and 54 kg/s, the shaft dimensions of 6.25 and 3.05 m diameter for the AIS and SHS, and 5 and 10 MW fire output estimates.

temperatures, by 1108 the measured outlet SHS temperature rose to about 29°F from the 25°F that was measured at 1048). The analysis stops at 11:13 PM on the evening of February 5.

Figure 9 shows the predicted mass flow rate and temperature at the bottom of the SHS for the time interval between the fire onset and the end of the analysis. The model does not consider acceleration required to turn the airflow around. Predicting the flow reversal process is further complicated by the fact that buoyancy effects (Eq. 2) handily exceed friction (Eq. 1) and there is considerable uncertainty in the precise thermal conditions in the shaft.

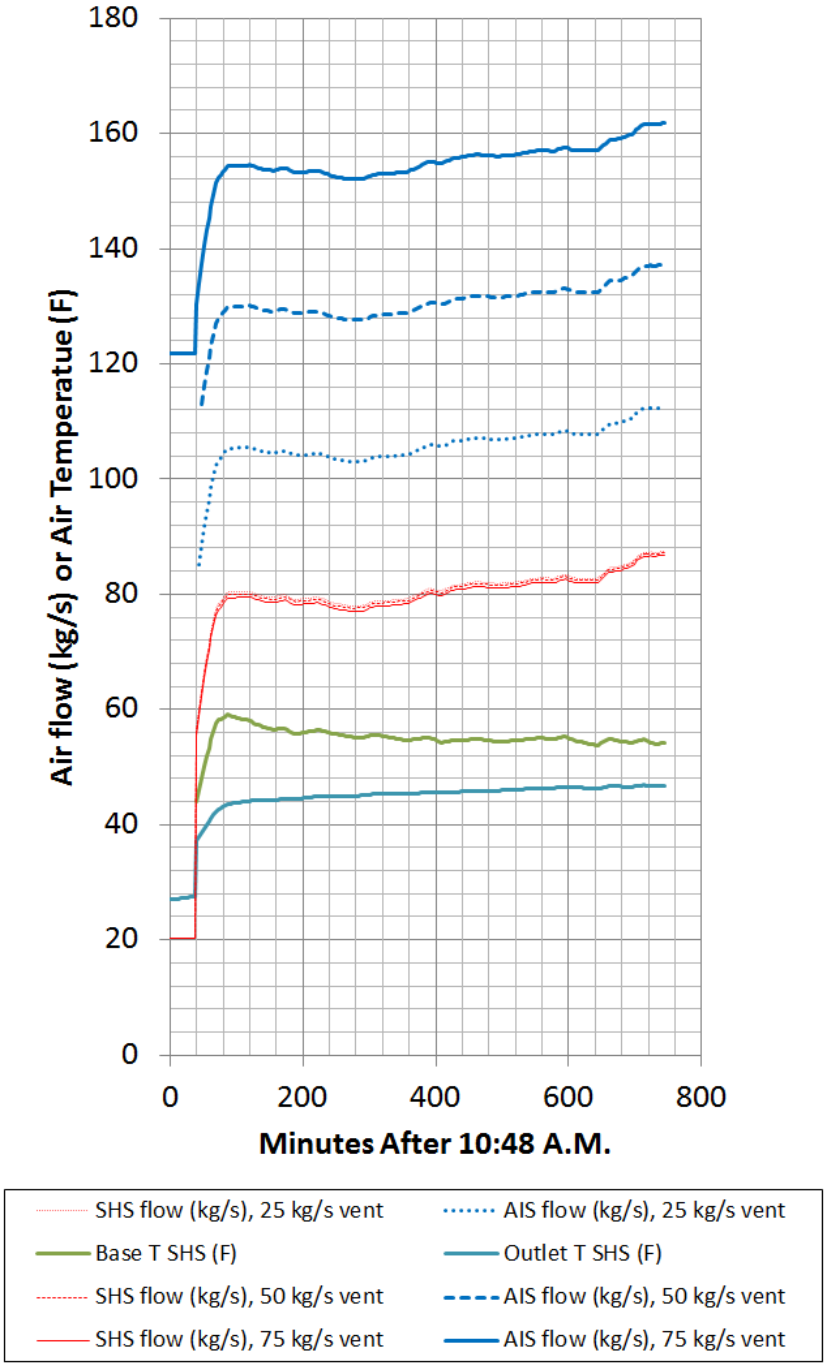

Figure 9: Post-fire predicted mass flow rates and temperatures

The predicted mass flow rate in the SHS shown in Figure 9 is fairly constant around 80 kg/s once the flow is established. The three red lines, corresponding to the different ventilation flows, are nearly indistinguishable. The calculated mass flow up the SHS falls slightly with higher ventilation flow because the increase in total flow in the AIS results in a slightly greater friction loss in that shaft. The three blue lines are the predicted flows for the AIS. As required by conservation, they are 25, 50, and 75 kg/s higher than the corresponding predictions for the SHS. The predicted inlet temperature for the air upcasting through the SHS is surprisingly low.

Figure 10 shows the model-predicted temperatures of the air and the confining shaft wall at 1148. The model predicts that air arriving at the bottom of the AIS has been warmed by the shaft from about 28ºF to 32ºF. The SHS is warmer as required for the buoyancy difference to counter friction and exit losses.

It may have taken some time for the flow reversal to develop. The slowing of the mine ventilation system probably gave the flow reversal up the SHS a kick-start. As noted earlier, the temperature at the SHS exit begins to rise minutes after the ventilation mode adjustment was ordered. Just prior to switching to ventilation mode the predicted mean flow speed in the AIS is 3.1 m/s while that in the SHS is 2.15 m/s. Since the bottom of the SHS and AIS are relatively close, they should have experienced roughly the same transient pressure in response to switching to ventilation mode. Consequently, flow in the two shafts should have experienced approximately the same deceleration. So when the flow went from 142 kg/s to $\dot{m}_{vent}$ kg/s, ignoring density variations, conservation requires:

$$(V_{AIS}A_{AIS} + V_{SHS}A_{SHS})\dot{m}_{vent}\,/142 = (V_{AIS} - \Delta V)A_{AIS} + (V_{SHS} - \Delta V)A_{SHS} \qquad (9)$$

where ΔV is the decrease in speed in both shafts. For the foregoing conditions, $\Delta V = 2.15$ m/s, just enough to stop the flow in the SHS, when $\dot{m}_{vent} = 37$ kg/s. While details of the transients in mine flow are not known, it seems plausible that the flow might have been arrested to $\dot{m}_{vent} < 37$ kg/s and the reversal initiated. The added bit of buoyancy due to the fire heating could then complete and sustain the reversed flow.

Figure 10 shows the predicted vertical variation in the temperatures of the air and the walls in the two shafts an hour after the fire onset. The wall temperatures are primarily established by the 4 and half days of interaction with the ambient air prior to the February 14 fire (Figure 5).

Figure 11 shows predicted temperature profiles for radial depth into the shaft walls at one hour after the fire onset at the top and bottom ends of both the AIS and the SHS. For both locations of the AIS the wall temperature has been falling (it is lower than the temperature at greater radial depth) because the ambient temperature at the time of the fire was ~30°F lower than it had been the previous day (Figure 5). At the bottom of the SHS the wall temperature is "turning around." It is warming up because higher temperature air is entering that end of the SHS.

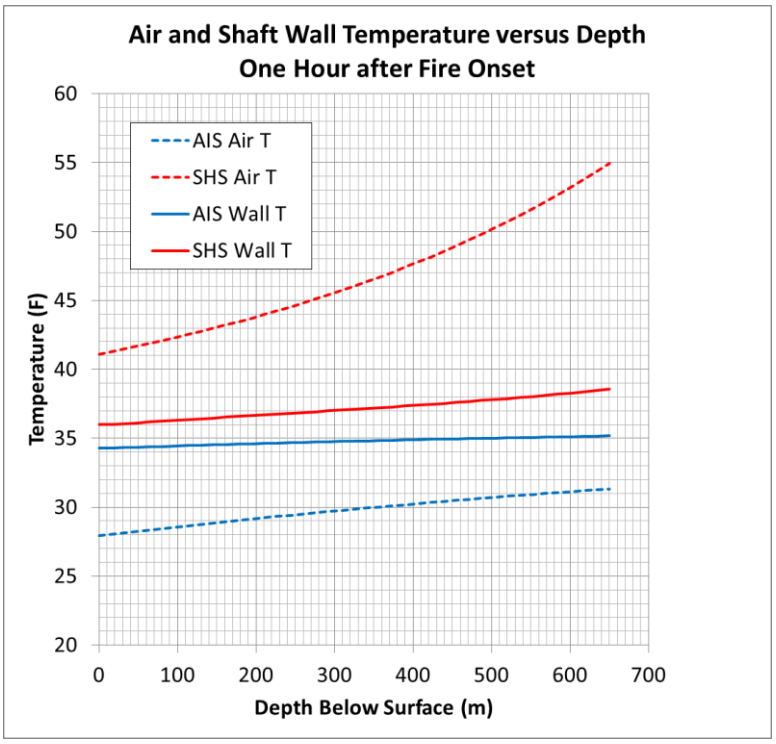

Figure 10: Vertical temperature profiles: air and shaft wall temperatures in AIS and SHS one hour after fire onset

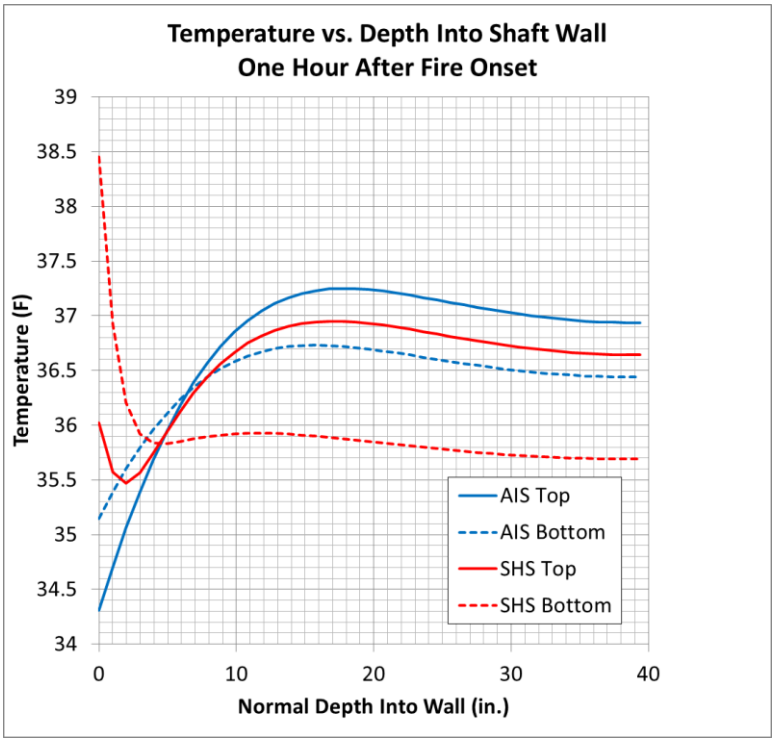

Figure 11: Predicted temperature versus depth into wall at tops and bottoms of AIS and SHS one hour after fire onset

Alternate Flow and Temperature Estimates for the SHS

As noted in the previous discussion (Figure 9), the temperatures predicted at the base of the SHS seemed low. The analysis of the previous section found the mass flow and temperature at the base of the SHS that allowed a pressure balance and matching of the temperature at the outlet of the SHS. The energy required of the fire to arrive at the temperature required at the base of the SHS was not considered. In this section an alternate approach is considered in which energy from the truck fire, less losses, is added to the air flow from the AIS. Figure 12 provides graphical solutions for conditions considered.

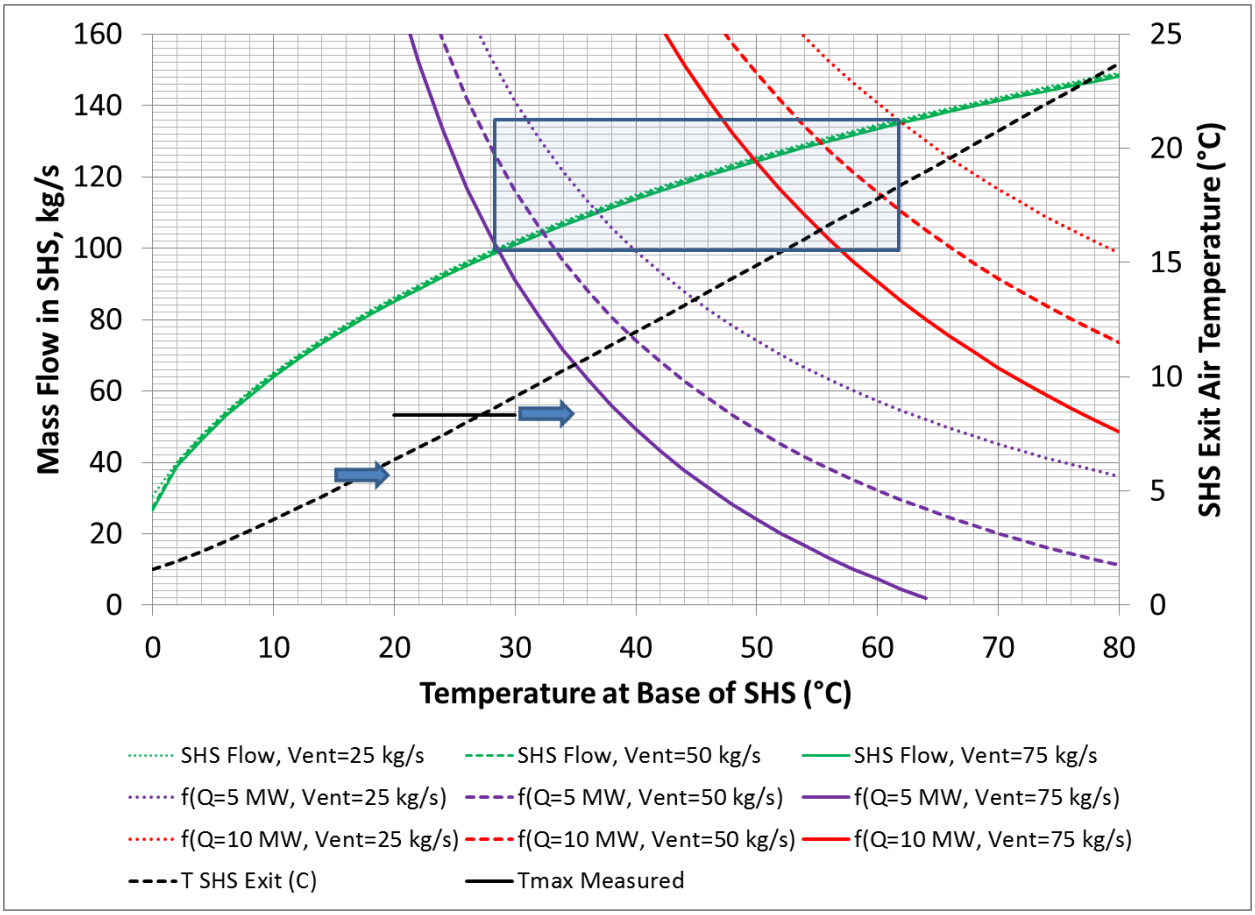

Figure 12: Predicted buoyancy-driven flows and 1st-law consistent flow for specified SHS base temperatures

In Figure 12, the green lines represent the mass flow calculated for the SHS using a specified temperature at the base of the SHS. The flow rate is that which satisfies the earlier momentum and energy equations for both shafts with the same pressure at their bases. The mass flow in the AIS is that of the SHS plus the ventilation flow. As before, the post-fire ventilation flow is 25, 50, or 75 kg/s. The wall temperatures of both shafts' are approximately those given in Figure 10. The three green lines corresponding to the different ventilation flows are nearly indistinguishable, but are ordered appropriately. The calculated mass flow up the SHS falls slightly with higher ventilation flow because the increase in total flow in the AIS results in a slightly greater friction loss in that shaft.

The dashed black line (Figure 12) is the estimated air temperature at the outlet of the upcasting SHS. The maximum measured SHS outlet temperature before the flow reverses again (11:13 PM on Feb 5, Figure 4) is shown as the solid black line segment. The intersection with the dashed line at about 27°C is the highest SHS base temperature that does not exceed the maximum measured temperature on the top end.

Details of the fire temperature spatial distribution are not considered, rather the region between the AIS and SHS is idealized as well-mixed and the air within as isothermal. Undoubtedly, a considerable temperature drop occurs in flow proceeding from the fire past the bottom of the SHS. Losses from radiation, in particular, would go up dramatically in high temperature regions. Consequently, the well-mixed average is expected to be between the hottest (near fire) and coolest (near SHS) parts of the actual system and thus constitutes a conservatively high estimate of the temperature at the SHS.

The red and purple lines are first-law consistent temperature predictions corresponding to fires of 10 and 5 MW thermal output. The dotted, dashed, and solid lines correspond to 25, 50, and 75 kg/s vent flow rates. The conservation of energy statement is:

$$Q_{\text{fire}} - Q_{\text{radiation}} - Q_{\text{convection}} = \dot{m}_{AIS} C_p (T_{SHS} - T_{AIS}) \tag{10}$$

where Q_{fire} is a specified thermal output of the fire (5 or 10 MW). Eq. 10 is used to solve for $\dot{m}_{AIS}$ for the two thermal powers and the varied ventilation rates as a function of T_{SHS}. Then

$$\dot{m}_{SHS} = \dot{m}_{AIS} - \dot{m}_{Vent} \tag{11}$$

$Q_{\text{radiation}}$ and $Q_{\text{convection}}$ are energy losses due to radiation and convection. The region between the bottom of the AIS and SHS was approximated as a rectangular box 30’ wide by 13’ high by 300’ long for which a mean beam length is $l = \frac{4V}{A} = 5.36$ m. The shaded box super-imposed on the Figure 12 encloses the estimated range of base SHS air temperatures and resultant SHS flows corresponding to 5-10 MW fire output and 25-75 kg/s ventilation flows based on the solutions of Eq. 10.

Conservatively small losses of energy from the air to the walls have been used. Larger estimates of $Q_{\text{radiation}}$ and $Q_{\text{convection}}$ would drive the shaded box in Figure 12 along the predicted (green) mass flow line closer to the origin and closer to agreement with the initial analysis (for which the SHS exit air temperature was required to match the measurement). Additional water evaporated from confining wall s and water and CO_2 from combustion would all enhance heat losses but are not considered in this model.

Soot from the fire would surely have been important in determining radiant losses from the hot products, but determining the transient and spatial variation of the soot properties is not practical. Moreover, the transient radiation through the varying conditions is not amenable to prediction. In addition to soot, H_2O and CO_2 would have been present and would have made contributions to radiation from gaseous products to the confining walls. To simplify the radiation prediction, only radiation from water vapor is considered here and only the water from the inlet air humidity is considered. That is, water added to the flow from combustion products is omitted. These very limiting assumptions still admit significant radiant losses and are sufficient to demonstrate that very significant cooling of the fire’s products and the mixing air will occur before the flow reaches the SHS. Based on surface conditions at the time of the fire (~50% relative humidity and 27°F) the partial pressure of water vapor in the ambient air was about 0.00243 atm. Figure 13 provides emittance associated with water in a mixture of 1 atm total pressure. At the mean beam length of 5.7 m the path-partial-pressure product is 0.013 atm-m and from the figure, $\epsilon_{H_2O} = 0.075$ (marked with “+”) at the low end of the temperatures presented. $\epsilon_{H_2O}\sigma T^4$ is an estimate of the mean radiant flux on the bounding surfaces so that:

$$Q_{\text{radiation}} = (2570\ \text{m}^2) \times \epsilon_{H_2O}\sigma(T^4 - T_{\text{wall}}^4) \quad (12)$$

where the area is the total surface area of the enclosing volume and the wall temperature, $T_{\text{wall}} = 20°\text{C}$. The convection loss in Eq. (10) was estimated as:

$$Q_{\text{convection}} = (2570\ \text{m}^2) \times h \times (T - T_{\text{wall}}) \quad (13)$$

where $h = 2\ \text{W}\cdot\text{m}^{-2}\cdot\text{C}^{-1}$, a conservatively small convection coefficient.

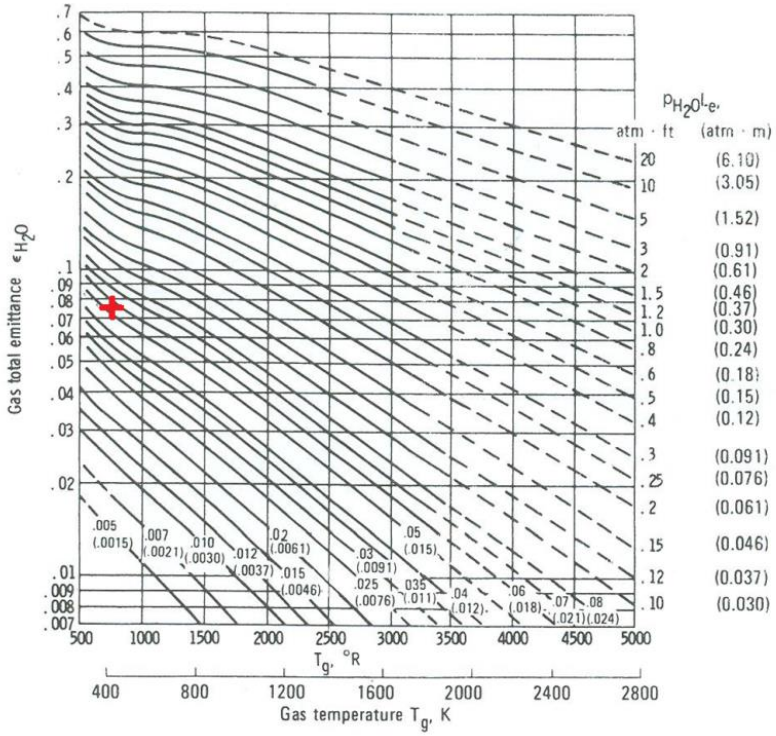

Figure 13: Total emittance of water vapor[8]

In Figure 12 the intersections of the red and purple lines with the green lines represent solutions to the conditions of conservation of energy per Equation 10 and the predicted mass flow balancing the buoyancy difference in the two shafts with friction losses. At the highest fire thermal output considered with the lowest ventilation rate (10 MW and 25 kg/s), this approach leads to an estimate of 62°C for the temperature at the base of the SHS. Note that the predicted SHS outlet temperature at this condition is very substantially higher than the measurement given in Figure 4. Consequently, 62°C is a conservatively high estimate of the temperature at the base of the SHS. For the ventilation flows of 50 and 75 kg/s the estimated SHS base air temperatures are 55°C and 50°C.

---

[8] Siegel, Robert, Howell, John R. "Thermal Radiation Heat Transfer" 4th ed. 2002. Taylor & Francis, New York, graph attributed to Hottel, H.C.: Radiant-Heat Transmission, in William H. McAdams (ed.), chap. 4, McGraw-Hill, New York, 1954.

Implications for Panel 7 Room 7 Thermal Disturbance

The previous section provides an analysis that demonstrates a temperature of less than 50, 55, or 62°C at the base of the SHS during the fire depending upon the ventilation rate. The flow downstream of the base of the SHS in the mine subsequently divides and only a portion of it goes through P7R7. The flow path from the SHS base to P7R7 is approximately an additional 4200 feet (1280 m). To provide a simple means of estimating the decrease in air temperature between the SHS base and P7R7 consider flow in a tube of constant wall temperature and with a constant convective coefficient. The downstream temperature, $T(L)$, is given by:

$$\frac{T(L)-T_w}{T_1-T_w} = \exp\left\{\frac{-LPh}{\dot{m}C_p}\right\} \qquad (14)$$

where L is the downstream distance and P is the perimeter of the flow channel, T_w is the wall temperature and T_1 is the entrance flow temperature. When h is based on the Dittus-Boelter Equation for large Reynolds number (>~10^4), which is generally the case for flows of interest in this investigation, the magnitude of Eq. 14 increases with increasing mass flowrate. Consequently, for a given T_1, a conservative estimate of $T(L)$ is realized by assuming a larger flow rate. A bounding estimate of the temperature at P7R7 is given by assuming that all of the ventilation flow remains in one flow passage in transit to P7R7. Assuming 25, 50, or 75 kg/s mass flow rates with 62, 55, and 50°C values of T_1 proceeding 1280 m in a 9.1 m by 4.0 m (30 ft by 13 ft) of constant wall temperature of 20°C results in an estimated temperatures at P7R7 of 24.5, 25.0, and 25.0°C. While a stronger flow in Eq. 14 predicts a larger response, the conservation of energy arguments from the previous section require lower T_1 for higher flow. The three conditions all result in about a 5°C rise above the wall temperature. The Dittus-Boelter equation predicts a convective coefficient of 2.5-6.0 W/m^2/K for the specified passage size and these three flow rates.

Conclusions of Thermal Analysis

This analysis demonstrates that very significant buoyancy-driven flow in the SHS resulted from the fire. Assumptions of the analysis were made to provide a conservatively high estimate of temperature at the base of the SHS. That the 62°C estimate is an upper bound is strongly supported by the measured air temperature at the SHS exit. In fact for this temperature the predicted SHS exit temperature is well higher than the measurement.

Conservatively small estimates of radiation and convection loss between the fire and the SHS base are sufficient to be consistent with the 62°C estimate for a 10MW fire. Using the assumption that the entire flow proceeds from the base of the SHS to the waste array, results in a 5°C predicted air temperature increase at the waste array.

Humidity Analysis

Humidity Increase in P7R7

The fire may have produced up to about 300 kg of H_2O products in 20 to 40 minutes time. Figure 5 is a plot of Carlsbad weather conditions in the time interval following Feb 5, 2014. At most the surface humidity was around 80% relative humidity at 30F at the time of the fire which corresponds to a humidity ratio of 0.0027 kg moisture per kg of air.

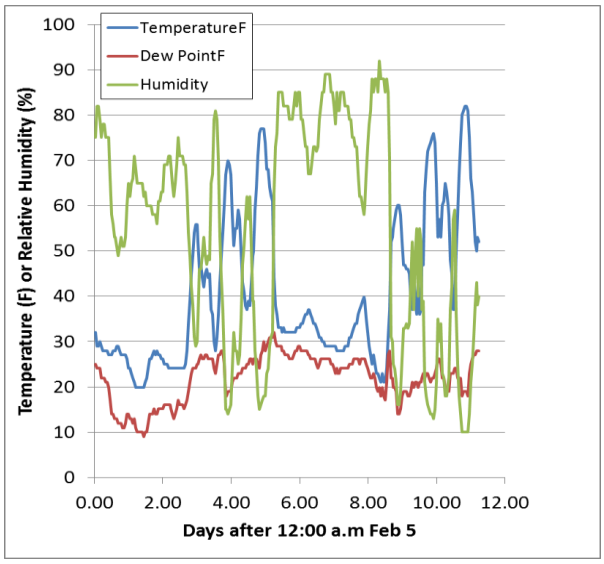

Figure 14: Carlsbad weather conditions between fire and release events

If 300 kg of water were produced in 20 minutes the production rate was 0.25 kg/s. Figure 12 summarized conservative conditions for estimating a relatively high temperature at the base of the SHS. In order to be conservative in estimating the effect of humidity, consider the relatively low mass flow corresponding to the condition that matched the SHS outlet temperature, i.e., 53 kg/s up the SHS. Additional flow is associated with ventilation through the mine, but adding the 0.25 kg/s just to the 53 kg/s airstream would raise the humidity ratio to 0.0074. The humidity ratio for saturated 20°C air is 0.01469. Therefore, at points away from the fire, there would not be condensation on 20°C walls. At distant points the air will be very near the salt wall temperature. If that is 20 °C, the 0.0074 humidity ratio corresponds to 51% relative humidity.

Note that the humidity discussion of the previous paragraph regards that of the incoming air as altered by water from the combustion process and does not consider interaction with the mine surfaces. The vast surfaces of the mine and equilibrium with natural moisture at the boundary are likely determining factors for humidity in the mine. Nonetheless, disregarding the wall interaction, it is evident that the flow was not saturated by the water addition even when cooled back to mine temperatures.

Exothermic Reactions of H_2O and CO_2 with MgO[9]

Because MgO hydration and carbonation generate heat, the likelihood of either reaction contributing to the February 14 radiation release from WIPP must be established. The relevant reactions are:

$$MgO + H_2O_{(l)} = Mg(OH)_2;\ \Delta H_{hydration} = -81.5\ kJ/mol,\ C_{p,hydration,298} = 37.2\ J/mol\ K$$

$$MgO + CO_{2(g)} = MgCO_3;\ \ \Delta H_{carbonation} = -101.\ kJ/mol\ C_{p,carbonation,298} = 75.6\ J/mol\ K$$

The magnitude of the enthalpies and heat capacities suggest that both hydration and carbonation could prompt temperature increases of several hundred ^{o}C, if reaction rates were not limited by: 1. slow reaction kinetics; 2. availability of H_2O or CO_2 including transport through the MgO bags, and/or; 3. heat transport away from the reaction site.

[9] Contributed by Patrick Brady, Senior Scientist, Org. 6910, Sandia National Laboratories

MgO hydration could occur by contact with liquid water or water vapor. Interviews with Sandians (L. H. Brush and C. R. Bryan) who did MgO kinetics analysis in the early 2000's, and a former Sandian (J. L. Krumhansl) who did earlier MgO kinetics analysis suggest that MgO hydration and carbonation are slow at the low temperatures and relative humidities prevalent in the WIPP. MgO carbonation is much slower than hydration[10]. Consequently, heat generation by MgO hydration is emphasized below.

Sandia[11] performed inundated and vapor hydration of MgO in the early 2000's. Note that these measurements were made on an earlier MgO provided by Premier Chemicals. The MgO used in P7R7 is a newer MgO with a smaller grain size. For the time being, the Premier MgO results are used to bound the reactivity of P7R7 MgO. Most MgO contains 1-3% CaO and 7-9% non-reactive silicate and aluminate impurities. Because hydration of CaO occurs very rapidly[12]; it is unlikely that unhydrated CaO existed in the Room 7 MgO. CaO hydration is therefore neglected here.

MgO hydration rates increase with temperature and relative humidity. Temperatures in the unventilated room would not have exceeded 28°C, the ambient temperature in the repository. The ambient relative humidity of the WIPP is 74%. After the truck fire on February 5 the humidity in P7R7 might have been increased due to the H_2O generated by the truck fire that occurred on February 5. The results of Snider[11] (slide 22) indicate that the hydration rate of MgO at 25°C is ~ 0.1 mol%/day (RH = 95%) and 0.025 mol%/day (RH = 75%). Because the Premier MgO was replaced by a finer grained MgO with presumably a higher surface area, these rates are likely minimum values. This assumes that MgO hydration is a surface-controlled process and that higher surface areas will prompt higher reaction rates.

Therefore, for the purposes of bounding the process, we assume that the hydration rate of MgO in P7R7 is twice the Premier MgO values; Rate = 0.2 mol%/day (RH = 95%) and 0.05 mol%/day (RH = 75%). Assuming free access of H_2O (no H_2O barrier performance of bags) and negligible heat loss, a maximum temperature rise of between 1 and 4°C is predicted using the following equation:

$$\Delta T = 0.01 * \text{Rate (mol\%/day)} * \Delta H_{hydration} / C_{p,hydration,298}$$

Possible temperature rises due to energy generation at these rates would easily be mitigated by heat losses to the air within the waste array and room. Consequently, these calculations suggest that MgO hydration is unlikely to have generated enough heat to melt the MgO bags.

Source of Damage to MgO Bags

A significant "footprint" of damage to the MgO bags and slipsheets was observed during the visual inspection of the waste pack array on May 30, 2014. The objective of these analyses was to evaluate any heat/mass transport scenarios that may have contributed to the damage to the MgO bags and the slipsheets.

---

[10] A.C. Snider, personal communication

[11] Snider, A. C. Hydration of Magnesium Oxide in the Waste Isolation Pilot Plant, Mat. Res. Soc. Symp. Proc. Vol. 757, 2003

[12] C. R. Bryan, personal communication

Potential for Thermal Damage to MgO Sacks

There are two plausible mechanisms by which the polypropylene super sacks could fail in the way observed in P7R7. They could either have 1.) ignited and burned or 2.) melted. Experiments show that the polypropylene readily ignites and sustains burning when exposed to even a small flame [Appendix F]. This is the most likely mechanism for the damage observed to the bags. It is also possible for the bags to melt due to an external heat flux such as a convective flux from hot gases and/or a radiative flux from a flame at a distance. Figure 15 shows a finite element model of the hexagonal blocks of MgO powder that was constructed to assess the combinations of incident heat flux and time required to heat the surface of the MgO to temperatures high enough to damage the polypropylene sacks.

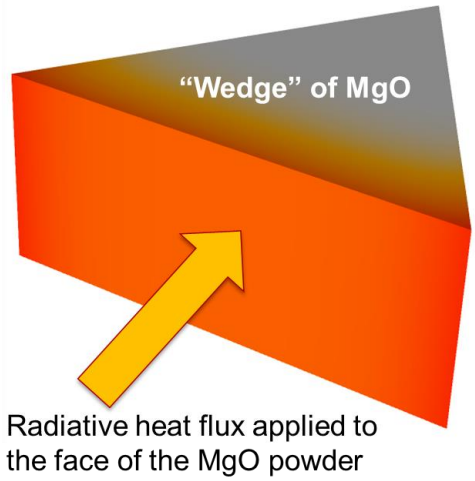

Figure 15: Illustration of finite element model of MgO sack

The polypropylene material will melt at approximately 400K. It is expected to lose structural integrity at lower temperatures. Experiments to determine the point at which mechanical failure would occur due to the pressure of the MgO powder and elevated temperature were discussed. It was decided that these experiments would not be performed due to time constraints and the high flammability of the polypropylene material suggesting that it is likely the bags burned rather than melted.

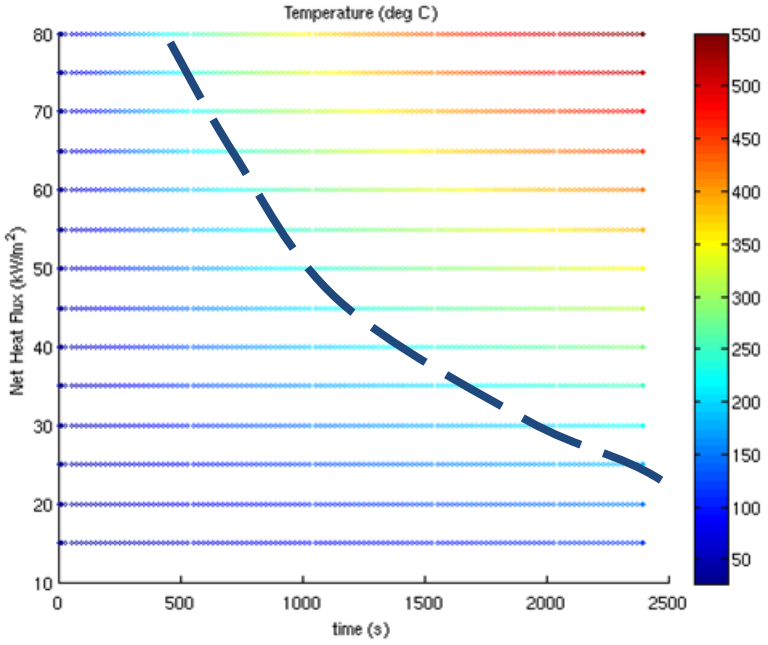

Figure 16: Bag surface temperature as a function of incident heat flux and time

The predicted surface temperature as a function of net heat flux and time is summarized in Figure 16. The dashed line indicates the relationship between the magnitude of the net heat flux and the approximate time for the bag to melt. For example, the polypropylene would melt after approximately 45 minutes of being subjected to a heat flux of 15 kW/m^2. This is the net heat flux which could consist of a combination of convective and radiative loads.

The damage footprint observed in P7R7 could be the result of multiple processes. It is possible that a fast release of flammable gases caused a fireball which damaged the MgO bags and ignited other combustible solids. These solids have been shown to be capable of sustaining flame once ignited and this flame could have propagated throughout the waste array. P7R7 was not inspected until several days following the release event. This flame propagation could have expanded the observed damage footprint over that time. Alternatively, the damage footprint observed in P7R7 could be the result of a sustained release of hot gases from drum 68660 over the course of several minutes. The validity of this second scenario is investigated here.

Accumulation of Flammable Gases within the Waste Array

One scenario in which the contents of the drums could have been heated by an external heat source was through the potential collection of flammable gases within the waste array and the subsequent ignition by an unidentified ignition source. To address this question, two scenarios were analyzed:

- Could heavier-than-air flammable gases "settle" within the voids of the waste array and subsequently been ignited?
- Could the air flow patterns within the room and waste array result in "stagnant" regions in which flammable gases (not restricted to heavier-than-air) could have collected within the voids of the waste array and subsequently been ignited?

To address the question of "heavier-than-air" gases, an estimate of the composition of the off-gas products of the chemical reactions within drum 68660 were computed by Hobbs[13] based on equilibrium of the products. In general, the dominate species of the products, which are assumed to have been vented from the drum, were H_2O, CO_2, CO, H_2, and CH_4. Based on these analyses, there were no heavier-than-air flammable gases venting from drum 68660 that would have collected within the waste array. Consequently, because the expected venting gases are not heavier than air, it is unlikely that these gases would have accumulated within the waste array due to their density. More likely, these flammable gases would have mixed with the bulk air through the room and be advected from the waste array. Additionally, the lack of an identified source of ignition also makes this scenario unlikely.

The question of flammable gases accumulating within the waste array due to recirculation regions of the bulk flow was considered. The largest challenge in addressing this question is the lack of knowledge of the actual geometry of the waste boxes, drum assemblies, and MgO sacks, as well as the geometric configuration of these assemblies/boxes within the waste array and the room. An accurate characterization of the waste array geometry is a necessary input to a numerical model intended to compute flow within and through the waste array. Initial consideration of this scenario was limited to scoping calculations with highly-simplified geometry and physical assumptions. As the belief that the breach and release was more likely to have occurred due to internal chemical reaction and heating, the pursuit of this possible external heating scenario became a lower priority. More detailed, higher-fidelity numerical models capable of resolving the flow within the waste array between the waste boxes, drum assemblies, etc. were not developed. This scenario also lacks an identifiable source of ignition.

Computational Fluid Dynamics (CFD) Energy Transfer

For this scenario, the damage footprint in P7R7 is expected to loosely correspond to the spatial domain that experienced significantly elevated temperatures during the release event. A computational fluid dynamics (CFD) model was constructed to estimate the spatial extent of the damage consistent with conservation of mass, momentum, and energy for plausible drum emission scenarios.

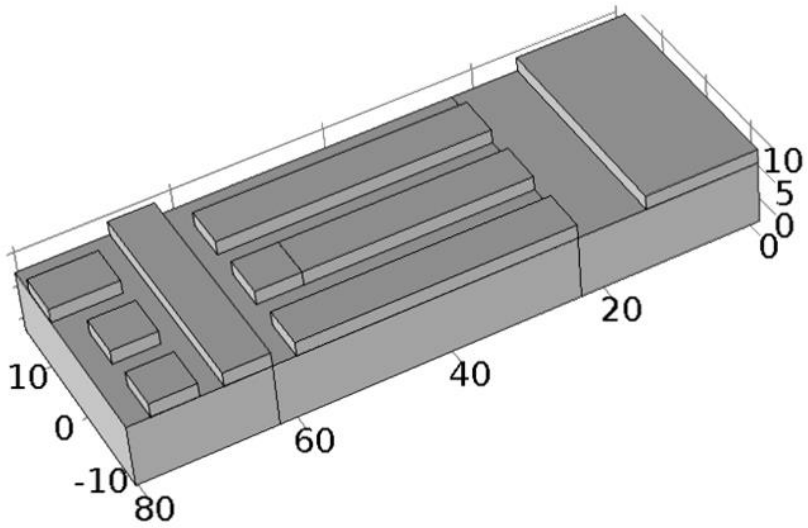

Figure 17: Approximate geometry of waste array in P7R7 (dimensions in feet)

[13] Hobbs, M.L., Cookoff modeling of a WIPP waste drum (68660), memo to Distribution, December 15, 2014.

An approximate geometry (Figure 17) is used for the CFD model. This simplification was made in order to reduce the mesh size and is justified by the fact that the precise arrangement of waste in P7R7 is uncertain. A consequence of this decision is that air flow through the waste array (expected to be near zero) is not simulated. The vast majority of the ventilation air flow is expected to go over and around the waste array. Additionally, because the geometry is approximate the simulation results are not expected to reproduce small-scale flow features.

There are a number of important parameters that are unknown which limits the utility of the simulation results. It is expected that results from the CFD model will become more useful as more information becomes available. With the limited data currently available, the CFD model predictions are useful in assessing if a proposed release hypothesis is plausible given the known damage footprint and the constraints of mass, momentum, and energy conservation.

The event duration is also uncertain. Shorter events are less likely to cause extensive damage. Longer event times (minutes) are considered. The burn rate and energy release of the waste is unknown. This is important because the speed/pressure at which the combustion products exit the drum has a large effect on the size and shape of the resulting plume of hot gases. The model does not adequately capture the geometry changes or the transient emission of hot gases due to the bursting of drum 68660. The model does not simulate the possible reaction or combustion of flammable gases exiting drum 68660. Instead, it is assumed that hot air exits the drum at a specified rate and temperature. The flow rate is chosen based upon 'reasonable' estimates for release duration and the total mass of ejected material. The temperature is chosen based on the analysis of the drum contents and the cook-off modeling (Hobbs) to be between 1000 and 1700K. The consequence of not modeling the combustion of the gases is that the model does not predict which surfaces would be exposed to direct flame in a given release scenario. The model also does not include the additional heat potentially generated due to the combustion of other materials in P7R7 such as slip sheets and polypropylene super sacks. The heat transfer to the solid surfaces is treated in an approximate manner. Conduction into these solid bodies is not directly simulated by the CFD numerical model and thus the effects of the transient response of the solids can only be estimated. Two bounding cases for the heat transfer between the fluid and solids are considered. To establish an upper bound on temperatures within P7R7 heat transfer between the fluid and solids is neglected. To establish a lower bound on temperatures in P7R7 a convection boundary condition is used but the wall temperature is held fixed at the initial condition. The k-ε turbulence model is used in all cases.

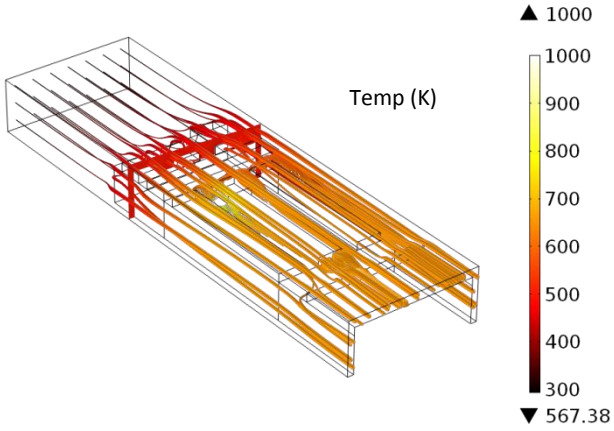

Figure 18: Results of CFD simulation (upper temperature bound)

Because of the low residence time for air in P7R7 relative to the expected release duration, steady-state results are presented. This sustained release scenario is further supported by the discoloration and

hardening of the MgO powder above drum 68660 consistent with extended exposure to NOx. The consequence of the above approximations and assumptions is that the results of the CFD analysis should currently be viewed as qualitative rather than quantitative. The ventilation flow rate through P7R7 was dramatically reduced when the HEPA filters were engaged in response to the release. This reduction in flow rate occurred approximately 10 minutes after the release event. Because the duration of the release event is unknown and is potentially greater than 10 minutes both the high (initial) and low ventilation flow rates are considered. Figure 18 shows the results for a release temperature of 1000K and a hot-gas mass flow rate of 3.3 g/s during the high ventilation condition. Sufficiently elevated temperatures are observed over the entire damage footprint. While higher temperatures and faster release flow rates are possible, they would only serve to further increase the temperature predictions. These temperatures are expected to be an overestimate because heat losses to the walls and room contents are neglected. The high-bias of predicted temperature is expected to be especially pronounced further from the release location.

To establish a lower bound on the temperature environment in P7R7, heat losses to the walls and waste are overestimated. This is done by using a convection coefficient boundary condition but not allowing the wall temperature to increase. For the illustrated case the maximum release temperature of 1700K and release flow rate of 33 g/s is used. Combined with the low ventilation flow rate these results are expected to represent the maximum temperatures achievable using this boundary condition.

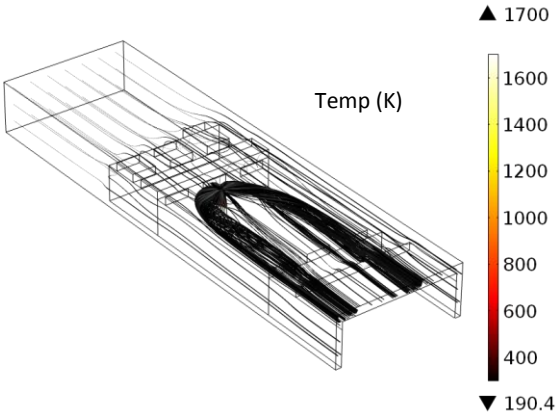

Figure 19: Results of CFD simulation (lower temperature bound)

Figure 19 shows temperatures over the damage footprint that would be too low to thermally damage the polypropylene sacks. The actual behavior at the interface between the air and solid surfaces is expected to be in between what is predicted by the two boundary conditions considered. Because the temperatures predicted using the conservatively low boundary condition would be insufficient to cause the observed damage even in the most damaging release scenario and the temperatures predicted by the adiabatic condition would easily suffice for even the least damaging release scenario we are forced to conclude that the damage observed in P7R7 may or may not have been solely caused by thermal effects. Further refinement of the upper and lower bounds may provide additional clarity, but is not a high priority activity. It is expected that thermal effects contributed to the damage but were likely not the sole cause. Mechanisms such as combustion in the room, flame propagation, burning drips of melted polymer and hot solid ejected material from the drum may also have contributed to the spreading of thermal damage.

Reduced Ventilation

Examination of the waste array geometry (Figure 20) reveals the waste containers to be very tightly packed. Many waste drums are contained in Standard Waste Boxes (SWBs), Standard Large Boxes (SLB2s) and 10-Drum Overpacks (TDOPs) further restricting airflow around the waste drums. These containers are vented to avoid pressurization in transit but the air within them is essentially stagnant and would be unaffected by changes to the ventilation in P7R7.

Drum 68660 is contained in a 7-pack. It is packaged closely with 6 other drums with polyethylene slip sheets above and below. The 7 drums are wrapped in cellophane further restricting air flow.

Figure 20: Waste Face at Panel 7 Room 7

The surface temperature of a chemically active waste drum such as 68660 is expected to rise less than 1°C prior to ignition (Hobbs[14]). This small temperature difference is not expected to drive significant natural convection currents which could be affected by changes to ventilation in P7R7. If reduced ventilation were sufficient to initiate a radiological release event, similar drums packaged in SWBs would have likely ruptured prior to February 14. Therefore, it is concluded that the reduction in ventilation in P7R7 due to the truck fire event would have had a negligible impact on the heat transfer environment of drum 68660 and is unlikely to have triggered the release event.

Duration of the Release

This analysis is an attempt to infer the duration of the release event. The analysis is in two parts: 1) the transient record from CAM151 is considered and 2) the activity of filters changed at stations A and B at the surface in the days following the release is examined.

The first part of the analysis looks at the transient record recorded by CAM151. Subsequent to completion of an initial analysis, it was learned that CAM151 stopped functioning around midnight of the day of the release. The analysis assumes perfect mixing of a representative sample of the material added to the ventilation air from the drum release. Turbulent diffusion in the flow-wise direction would stretch the time interval of a concentration passing CAM151. A calculation was performed that accounts for axial movement of the material due to diffusion. The analysis is complicated by the fact that the flow speed was promptly reduced by approximately a factor of 20 when the alarm was received. The signal from CAM151 endured for about 3300s. The analysis indicates that a continuous ten second

release results in a signal shorter than the CAM151 data while the 100s release clearly produces a longer signal. The consequence of the CAM151 signal ending is that this diffusion analysis cannot be used to suggest an upper limit to an interval of material release at Drum 68660.

A plot of the relative activity of filters removed from Stations A and B at the surface in the days following the release shows a very dramatic decrease in the count rate for about one and half days. After that interval of rapid decrease the count rate decreases much more slowly. Due to the large volume of the mine system and the large distance between the release and the filters a period of a day or so (several air exchanges) would be expected to entirely clear a well-mixed gas from the mine. The sharp decrease in filter load after 1.5 days implies that significant release of material ended at some point before that. Filter load in days following the initial 1.5 days was likely associated with slower processes re-suspending material deposited on mine surfaces.

CAM151 Analysis Considering Turbulent Diffusion in the Flow-wise Direction

Figure 21 shows the recorded signal from CAM151 which samples air leaving Panel 7. This sensor was the initial indication of the release on February 14. Based on Figure 21, it appeared that radioactive contaminant passed CAM151 for approximately 3300s. Reynolds numbers associated with flows in mine corridors indicate turbulent flow conditions. In the presence of such turbulence the diffusion of a contaminant in the flow-wise direction is many orders of magnitude greater than diffusion in quiescent air. Consequently, if there were a release of short duration at the waste array the "signal" 600 feet away at CAM 151 would be "stretched." This analysis attempted to demonstrate that the release event was of short duration.

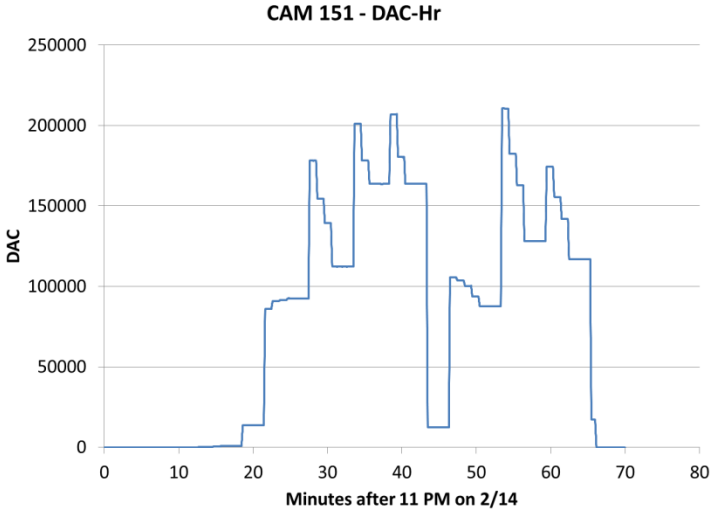

Figure 21: Transient Count Record from CAM151[14]

A turbulent diffusion calculation was used to estimate the degree to which material released into the air in P7R7 would diffuse in the flow-wise direction before reaching CAM151. The ventilation data indicated that the airflow through Panel 7 dropped promptly when CAM151 sounded off (Figure 22). This analysis uses superposition of an analytical solution to the 1-d advection/diffusion equation. The concentration (Socolofsky & Jirka) from a small release diffused and advected in one direction is[15]:

[14] U.S. Department of Energy Office of Environmental Management Accident Investigation Report, *Phase 1 Radiological Release Event at the Waste Isolation Pilot Plant February 14, 2014*, April 2014.

[15] S. A. Socolofsky and G. H. Jirka, "Chapter 2, Advective Diffusion Equation," [Online]. Available: https://ceprofs.civil.tamu.edu/ssocolofsky/cven489/Book/Book.htm.

$$C(x,t) = \frac{M}{\sqrt{4\pi Dt}} \exp\left(\frac{-(x-Ut)^2}{4Dt}\right) \tag{15}$$

In order to simulate a continuous constant release for an interval of time the total release can be divided into a series of N releases and the result of superposition used at the time and position of interest. Consider position L away from the constant source of duration T and represent the release as N small releases distributed over the time interval.

$$\dot{M} = \frac{M}{T} \tag{16}$$

$$C(L,t) = \sum_{i=1}^{N^*} \frac{M/N}{\sqrt{4\pi D\hat{t}_i}} \exp\left(\frac{-(L-U\hat{t}_i)^2}{4D\hat{t}_i}\right) \tag{17}$$

where

$$\hat{t}_i = t - (i - 0.5)T/N, \tag{18}$$

D is the diffusion coefficient, M is the total mass released[16], and U is the flow speed.

$$N^* = \begin{cases} N \text{ for } t \geq T(1 - 1/[2n]) \\ \text{INT}\left(\frac{Nt}{T}\right) \text{ for } t < T \end{cases} \tag{19}$$

The variable upper limit on the summing allows for investigation of times less than the duration of the release.

The foregoing is sufficient to estimate $C(L,t)$ for constant conditions. In the present case the release is occurring during an initial interval of $U = U_1$ followed by an interval of $U = U_2$ that occurs when $C(L,t^*) > C_{\text{detect}}$. This time, t^*, could be less or greater than the release interval T. In any case, at t^* the spatial interval $0 < x < L$ has an existing concentration distribution and the speed changes abruptly to U_2.

To continue past t^* in time we can represent the existing distribution as a spatially distributed series of releases that occurred at $t = t^*$. At position L for $t > t^*$:

$$C(L, t > t^*) = C_{\text{source}} + C_{\text{inventory}} \tag{20}$$

C_{source} is contribution from continued release at the source (this will be zero if the full release has occurred before t^*). If $t^* < T$ C_{source} is:

$$C_{\text{source}} = \sum_{i=N_1}^{N^*} \frac{M/N}{\sqrt{4\pi D\hat{t}_i}} \exp\left(\frac{-(L-U_2\hat{t}_i)^2}{4D\hat{t}_i}\right) \tag{21}$$

where N_1 is time position of the first release to occur after t^*. The time after the flow slows is:

[16] This one-dimensional system does not include the cross-sectional area so a unit of mass here is 1 gm/m^2. For each case studied a total of 1 gm/m^2 was released.

$$\tilde{t} = t - t^* \tag{22}$$

and the inventory in the pipe is represented as releases that occurred at $\tilde{t}$. So

$$C_{\text{inventory}} = \sum_{j=1}^{J} \frac{\delta x C(x_j, t^*)}{\sqrt{4\pi D\tilde{t}}} \exp\left(\frac{-([L-x_j]-U\tilde{t})^2}{4D\tilde{t}}\right) \tag{23}$$

where the "pipe" is broken into J segments and

$$\delta x = \frac{L}{J} \tag{24}$$

$$x_j = (j - 0.5)\delta x \tag{25}$$

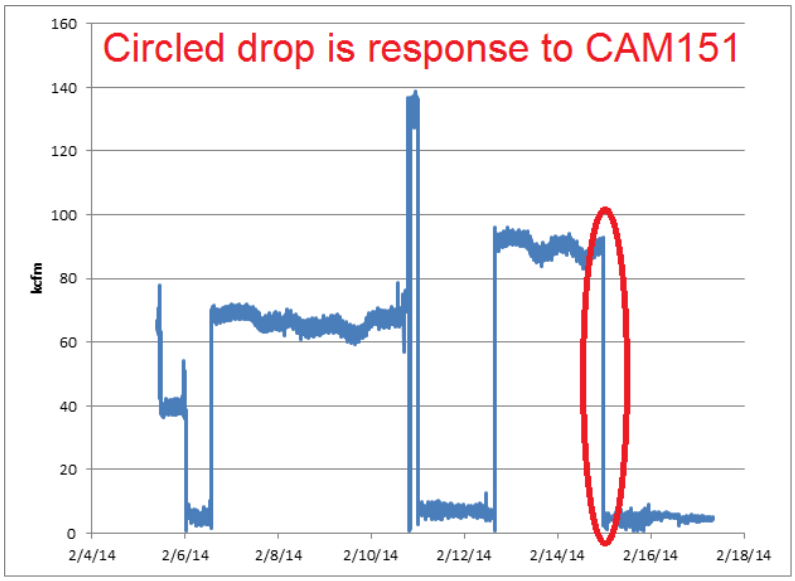

Figure 22: Plot of panel 7 airflow from Ted Wyka supplied spreadsheet[17] (Wyka)

Figure 23 presents a graph of $D_{xx}/(Ud)$ from various investigators [3] for turbulent pipe flows where D_{xx} is the turbulent diffusivity. The following table also summarizes the diffusivity for the two flow conditions based on the air flowrates shown in Figure 22.

Description	High Flow	Low Flow
Volumetric Flow	90.26 kcfm	4.35 kcfm
Mean flow Speed	0.872 m/s	0.0420 m/s
Reynolds Number	386,000	18,600
$D_{xx}/(Ud)$	0.121	0.263
D_{xx}	0.687	0.0721

[17] T. Wyka, *Email supplying underground airflow data at WIPP in response to action item generated at LANL meeting on Aug 18 and 19.*

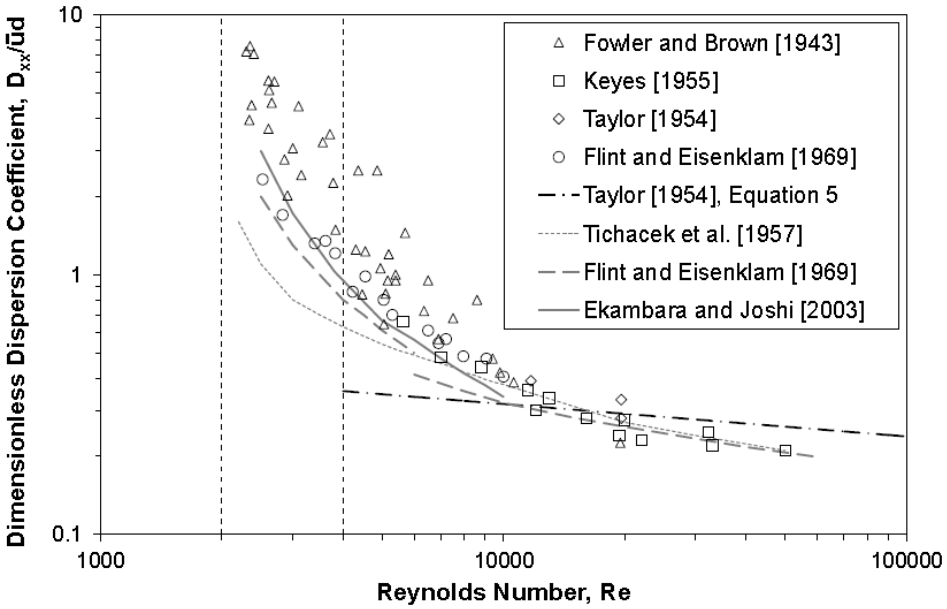

Figure 23: Summary of flow-wise dispersion coefficients from various investigators[18]

The superposition method was used to estimate the concentration history (in relative mass) at CAM151. An arbitrarily small detection concentration threshold was set at 1×10^{-4}gm/m^3 times. Figure 24 shows the predicted concentration histories at CAM151 for release times of 10, 100, 300, and 1000s At the time of detection the flow slows and the more complicated superposition solution (Eqs. 21 and 23) is used. For the short release times considered (10s and 100s) the whole release event has occurred before detection so $C_{\text{source}} = 0$. For the 300 and 1000s release times the character of the concentration estimate is rich and shows clear features due to both the inventory in the flow passage at t^* and the release that continues after t^*.

In all cases, the area under the predicted concentration curve conserves mass. That is:

$$U_2 \int_0^{8000s} C(L,t)dt = 1 \text{ gm/m}^2 \qquad (26)$$

Based on the assumptions of this model and the recognition of a very slow flow speed *immediately* following detection, flow-wise dispersion is very significant. An enduring release, say greater 200s, would be stretched out for several thousand seconds by the time it has slowly traveled from Panel 7 to CAM151. A rapid release, on the other hand, will contaminate a shorter interval of flow in the passage. Further, a greater fraction of a rapid release will have occurred before detection at CAM151.

[18] J. Hart, I. Guymer, A. Jones and V. Stovin, "Longitudinal Dispersion Coefficients within Turbulent and Transitional Pipe Flow," in *Experimental and Computational Solutions of Hydraulic Problems*, 32nd International School of Hydraulics, pp. http://link.springer.com/book/10.1007/978-3-642-30209-1 .

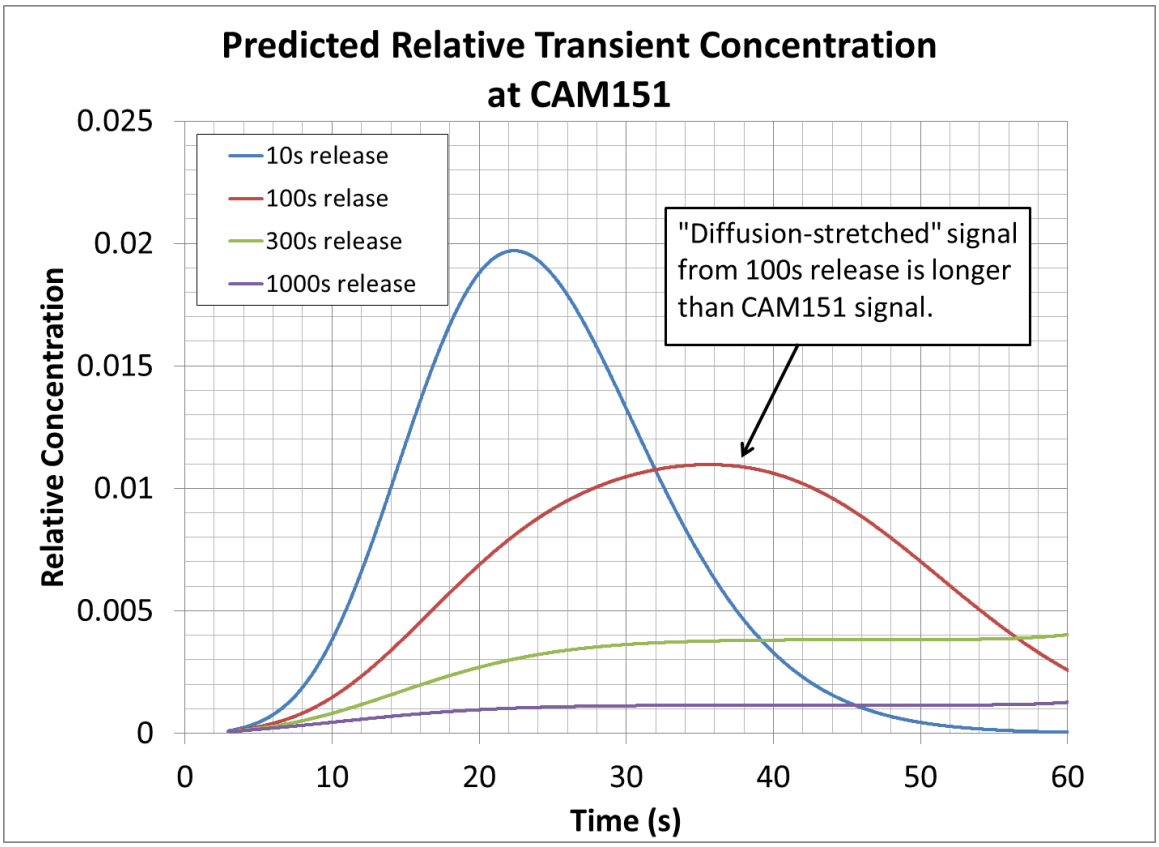

Figure 24: Predicted transient concentration at CAM151 for various release time intervals

The signal from CAM151 endured for about 3300s. As shown in Figure 24, the ten second release results in a signal shorter than the CAM151 data while the 100s release clearly produces a wider signal. As noted earlier, this analysis is substantially discredited by the likelihood that the signal end in Figure 21 is only due to the sensor stopping. Consequently, the radiological signal is not a clear indication of a short release duration from Drum 68660. Even if the release were very short the deposition and resuspension of the contaminant that may occur is complicated. The foregoing idealization is the simplest possibility.

Analysis of Filters A and B Activity in Days Following the Release

Figure 25 shows a plot of activity of filters for Stations A and B from the days after the release as document at the Department of Energy website[19]. The source document alludes to multiple methods of the filter analysis. Figure 25 presents the reported numbers without further consideration of the analysis method. The reported information gives time of analyzed filter removal. Figure 25 shows the activity per day of filter residence presuming no delay between the removal and installation of successive filters. The scatter plot makes clear that the radioactivity load in the filters drops orders of magnitude in a few days' time and then levels out. For the first couple of days the activity rate for Beta or Alpha at Station A and for Alpha at Station B drops by approximately an order of magnitude per day.

[19] http://wipp.energy.gov/special/ventilation%20System%20Sampling%20Results.pdf

It appears from this data that any radioactivity released in the mine was confined to a short (<~1 day) interval of time. The actual processes conveying released material from P7R7 to the surface filters was complicated. For a contaminant that remains well-mixed in a volume, the concentration decreases ten-fold for every 2.3 (LN(10)) exchanges of air. Of course, the WIPP mine system did not remain well-mixed between the release site and the exits which would delay the dilution process. Consequently, significant release must have been confined to a period of time short relative to one day in for the "signal" at the filters to decay several orders of magnitude in just the first few days.

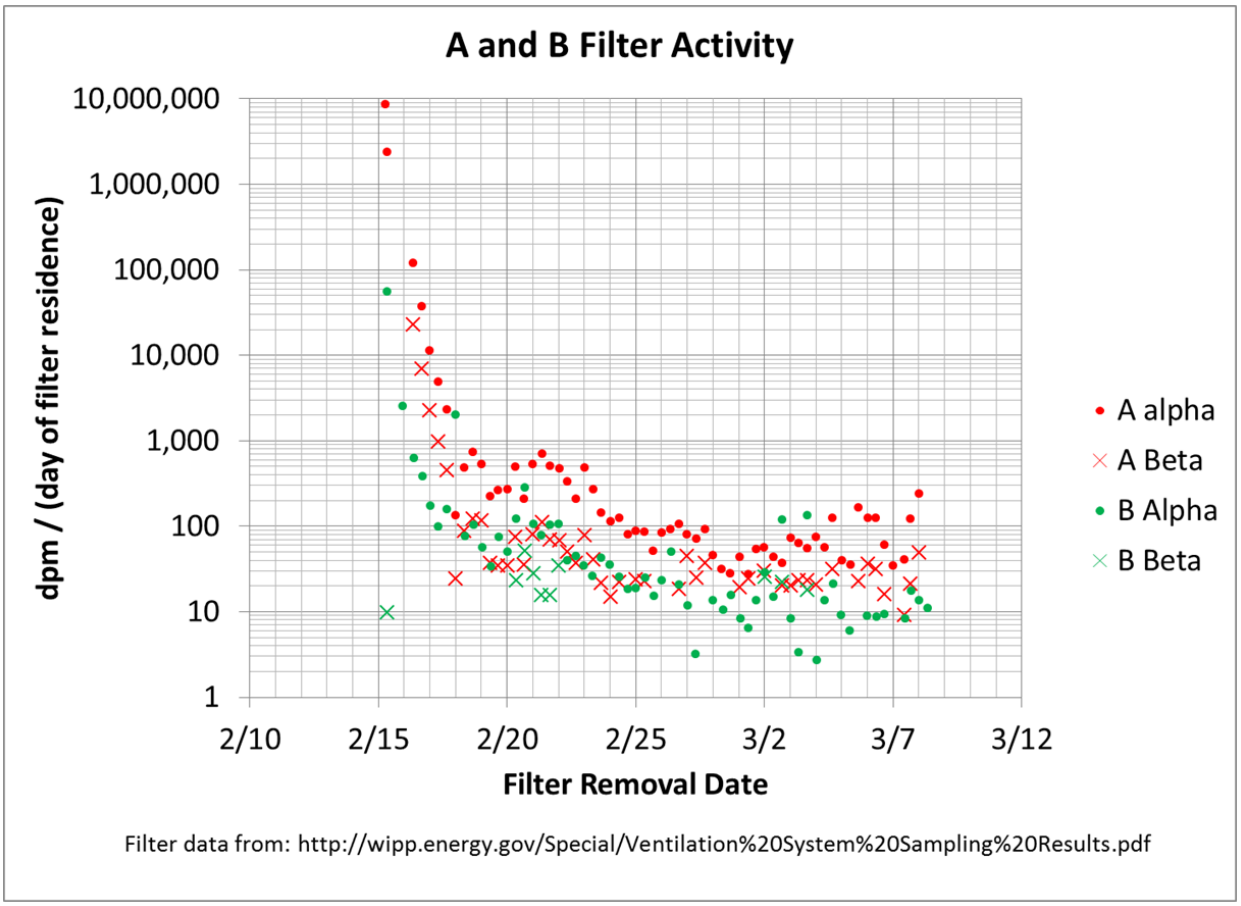

Figure 25: Beta and alpha counts from filters at the surface in days following the release

Conclusions

Thermal and humidity stimuli to the waste array resulting from the February 5 salt haul truck fire were considered and it appears that the release event of February 14 was not initiated by the fire. Other analyses examined the plausibility of important physics mechanisms that are consistent with the visual observations at the release site available through the early (May-June) inspections. It is plausible that hot issuing gaseous products from drum 68660 spread to the approximate known damage footprint. However, as MgO bags were demonstrated to be flammable, it is not necessary that the hot eruption cover the extent of the damaged area. Nothing discovered in these analyses contradicts the hypothesis that exothermic reactions in drum 68660 led to the release and the observed damage in the waste array.

Distribution

Sorensen, N. R., 1818, nrsoren@sandia.gov

Johannes, J. E., 1500, jejohan@sandia.gov

Hassan, B., 1510, bhassan@sandia.gov

Pilch, M., 1514, mpilch@sandia.gov

Hogan, R. E., 1514, rehogan@sandia.gov

Larsen, M. E., 1514, melarse@sandia.gov

Tencer, J., 1514, jtencer@sandia.gov

Geller, A. S., 1516, asgelle@sandia.gov

Redmond, J. M., 1550, jmredmo@sandia.gov

Smith, J. A., 1555, jasmith@sandia.gov

Minier, L. M. G., 2554, lminier@sandia.gov

Kaneshige, M. J., 2554 mjkanes@sandia.gov

Shoemaker, P. E., 6210 peshoem@sandia.gov